Imperfection sensitivity analysis of laminated folded plates

E. J. Barbero
West Virginia University, Morgantown USA
and
A. Madeo[1], G. Zagari, R. Zinno, and G. Zucco
University of Calabria, Arcavacata di Rende, CS, Italy

Abstract

A novel methodology for imperfection sensitivity analysis is presented. Koiter's perturbation method is used to calculate the imperfection paths emanating from mode interaction bifurcations, which occur on the post-buckling paths of the single modes. The Monte Carlo method is used to tests a large number of modes and all possible interactions among them. The computational cost is low because of the efficiency of Koiter's method. The demands of Koiter's method for accurate evaluations of higher order derivatives of the potential energy are met by a mixed, corotational element.

Keywords

Koiter, Composite, Corotational, Monte Carlo, Imperfection, Sensitivity

1. INTRODUCTION

The design of composite structures is most often dominated by buckling [1, 2]. For example, the demands for fuel efficiency is prompting the aircraft industry to revolutionize airframe construction to save weight, and thus fuel. A promising concept is to let the airframe operate in the postbuckling regime, where the skin of the composite stiffened panels are allowed to buckle in normal flight

[1]Corresponding author.

conditions. This hinges upon the assumption that stiffened panels, and thus the entire airframe, are imperfection insensitive.

Imperfection sensitivity analysis requires the identification of a large number of buckling modes and their interaction. Because of the large number of possible modes and our a priori ignorance about which ones would interact with each other, such analysis is prohibitively time consuming. Continuation methods based on Riks scheme are often used [3]. In spite of the simplicity of its numerical implementation, which requires only an approximation of the tangent stiffness matrix, the method suffers in the case of multiple bifurcations, requiring ad-hoc branch switch algorithms [4]. Continuation methods are time consuming, requiring a lengthy analysis for each assumed imperfection. Furthermore, type and shape of imperfections are unknown, either because the structure is in the design stage or because it is too difficult to measure them.

Therefore, the aim of this work is to propose a robust and efficient methodology to calculate the imperfection sensitivity of laminated composite folded plates, including stiffened panels as a particular case. The proposed methodology does not require a priori knowledge of the shape and magnitude of imperfections and does not rely on lengthy continuation analysis. Instead, it uses Koiter's perturbation approach [5, 6] to calculate the bifurcation load, post-buckling path, and interaction between modes to detect bifurcations on the post-buckling path of individual modes, as well as the paths emanating from those bifurcations. The requirement for linearity of the constitutive equations is easily met by composite materials, which have a broad, linear stress and strain range of operation in compression [7].

The most recent implementations of Koiter's approach include spatial beam assemblages [8], folded plates [9], and composite structures [10]. Since the approach is based on fourth-order energy expansion [8], a finite element capable of accurately representing fourth-order terms is required for robustness of the analysis. The corotational approach [11, 12] fulfils this requirement allowing the complete reuse of a linear element for geometrically nonlinear analysis. A mixed formulation is used to avoid extrapolation locking [13]. The recent 3D plate finite element [14] based on Hellinger-Reissner variational formulation guarantees an accurate evaluation of linear elastic response and of rotation fields [15], so it is very suitable to be used with a corotational formulation to obtain a geometrically nonlinear formulation, which is accurate up to fourth order energy terms [10, Fig. 3.b].

Koiter's method provides robust prediction of the path emanating form interaction bifurcations

between three or more modes, thus providing a good estimate of the imperfection sensitive, post-buckling trajectory (even when the shape and magnitude of the imperfections are unknown) that otherwise would be very costly to follow by a continuation methods. Mode interaction often produces the most deleterious imperfection sensitive path with the larger drop in load carrying capacity [16–18]. The difficulty resides on how to select the set of modes that produces the worst behavior.

The Monte Carlo method is proposed herein to find the modes that yield the most unfavorable, imperfection sensitive path. Although Monte Carlo is an expensive method, the computational cost is keep low thanks to the efficiency of both the element used and Koiter's approach. Also, Koiter's approach is quite demanding about the quality of higher order (up to 4th order) derivatives of the energy, but the element formulation used in this work is uniquely suited to satisfy those demands for accuracy at a low computational cost. The proposed methodology allows us to run thousand of analysis in a few seconds, obtaining the worst imperfection using a Monte Carlo simulation.

2. KOITER'S FORMULATION

2.1. The asymptotic analysis

Asymptotic analysis is essentially the implementation of Koiter's nonlinear elastic stability approach [5] into the finite element method (FEM) [6]. The solution process is based on an expansion of the potential energy Φ in terms of load factor λ and modal amplitudes ξ_i. It can be summarized as follows:

i.. The *fundamental path* is obtained as a linear extrapolation

$$\boldsymbol{u}^f[\lambda] = \boldsymbol{u}_0 + \lambda\hat{\boldsymbol{u}} \tag{1a}$$

where $\boldsymbol{u}_0$ is an initial displacement, possibly null, and $\boldsymbol{u} = \lambda\hat{\boldsymbol{u}}$ is the vector of kinematic parameters, i.e., the space of *degrees of freedom (dof)* of the structure, and $\widehat{\boldsymbol{u}} = d\boldsymbol{u}/d\lambda$ is obtained as the solution of the linear algebraic equation

$$\boldsymbol{K}_0\,\hat{\boldsymbol{u}} = \hat{\boldsymbol{p}} \tag{1b}$$

where $\hat{\boldsymbol{p}}$ is the reference load and $\boldsymbol{K}_0 = \boldsymbol{K}[\boldsymbol{u}_0]$ is the stiffness matrix, which contains the

coefficients of the quadratic terms of the energy Φ''.

ii.. A cluster of *buckling loads* λ_i, $i = 1 \cdots m$, and associated *buckling modes* $\dot{\boldsymbol{v}}_i$ are obtained along $\boldsymbol{u}^f[\lambda]$ by the critical condition

$$\boldsymbol{K}[\lambda_i]\,\dot{\boldsymbol{v}}_i = \boldsymbol{0} \quad , \quad \boldsymbol{K}[\lambda] = \boldsymbol{K}[\boldsymbol{u}_0 + \lambda\hat{\boldsymbol{u}}] \tag{1c}$$

the eigenvalue problem is defined as fully nonlinear, to correctly recover the post-critical behavior. The nonlinearity is introduced by updating the configuration along the fundamental path.

Note that the size m of the subspace of buckling modes needed for the analysis is orders of magnitude smaller than the number of dof used to discretize the structure, often as little as $m = 3$.

We denote by $\mathcal{V} = \{\dot{\boldsymbol{v}} = \sum_{i=1}^{m} \xi_i \dot{\boldsymbol{v}}_i\}$ the subspace spanned by the buckling modes $\dot{\boldsymbol{v}}_i$ (where ξ_i are the modal amplitudes) and by $\mathcal{W} = \{\boldsymbol{w} : \boldsymbol{w} \perp \dot{\boldsymbol{v}}_i\,,\ i = 1 \cdots m\}$ its orthogonal complement, defined by the orthogonality condition

$$\boldsymbol{w} \perp \dot{\boldsymbol{v}}_i \ \Leftrightarrow\ \Phi_b'''\hat{u}\dot{v}_i w = 0 \tag{1d}$$

where $\hat{u} = \mathcal{L}\hat{\boldsymbol{u}}$, $\dot{v}_i = \mathcal{L}\dot{\boldsymbol{v}}_i$, $w = \mathcal{L}\boldsymbol{w}$ and $\mathcal{L}$ is the linear operator of FEM interpolation.

We denote by λ_b an appropriate reference value for the cluster, e.g. the smallest of λ_i or their mean value. Accordingly, a suffix "b" denotes quantities evaluated in correspondence to $\boldsymbol{u}_b = \boldsymbol{u}^f[\lambda_b]$.

iii.. Defining $\xi_0 = (\lambda - \lambda_b)$ and $\dot{\boldsymbol{v}}_0 = \hat{\boldsymbol{u}}$, the asymptotic approximation for any equilibrium path is approximated by a expansion in terms of mode amplitudes ξ_k as follows

$$\boldsymbol{u}[\lambda, \xi_k] = \boldsymbol{u}_b + \sum_{i=0}^{m} \xi_i \dot{\boldsymbol{v}}_i + \frac{1}{2}\sum_{i,j=0}^{m} \xi_i \xi_j \boldsymbol{w}_{ij} \tag{1e}$$

where $\boldsymbol{w}_{ij} \in \mathcal{W}$ are quadratic corrections introduced to satisfy the projection of the equilibrium equation (see[19, Section 3.3]) into $\mathcal{W}$, obtained by the linear *orthogonal equations*

$$\delta\boldsymbol{w}^T(\boldsymbol{K}_b\boldsymbol{w}_{ij} + \boldsymbol{p}_{ij}) = 0\ , \quad \forall \boldsymbol{w} \in \mathcal{W} \tag{1f}$$

where $\boldsymbol{K}_b = \boldsymbol{K}[\boldsymbol{u}^f[\lambda_b]]$ and vectors $\boldsymbol{p}_{ij}$ are defined as a function of modes $\dot{\boldsymbol{v}}_i$; $i = 0 \cdots m$, by the energy equivalence $\delta \boldsymbol{w}^T \boldsymbol{p}_{ij} = \Phi_b''' \delta w \, \dot{v}_j \dot{v}_j$.

iv.. The following energy terms are computed for $i, j = 0 \cdots m$, $k = 1 \cdots m$:

$$\begin{aligned} \mathcal{A}_{ijk} &= \Phi_b''' \dot{v}_i \dot{v}_j \dot{v}_k \\ \mathcal{B}_{ijhk} &= \Phi_b'''' \dot{v}_i \dot{v}_j \dot{v}_h \dot{v}_k - \Phi_b''(w_{ij} w_{hk} + w_{ih} w_{jk} + w_{ik} w_{jh}) \\ \mathcal{C}_{ik} &= \Phi_b'' w_{00} w_{ik} \\ \mu_k[\lambda] &= \frac{1}{2}\lambda_b(\lambda - \frac{1}{2}\lambda_b)\Phi_b''' \hat{u}^2 \dot{v}_k + \frac{1}{6}\lambda_b^2(\lambda_b - 3\lambda)\Phi_b'''' \hat{u}^3 \dot{v}_k \end{aligned} \tag{1g}$$

where the *implicit imperfection factors* μ_k are defined by the 4th order expansion of the unbalanced work on the fundamental path, i.e., $\mu_k[\lambda] = (\lambda \hat{p} - \Phi'[\lambda \hat{u}])\dot{v}_k$ (see [19, Eqs.(31,32)]).

v.. The equilibrium path is obtained by projecting the equilibrium equation [19, Section 3.4] on $\mathcal{V}$. According to eqs, (1a)–(1g), we have

$$\frac{1}{2}\sum_{i,j=0}^{m} \xi_i \xi_j \mathcal{A}_{ijk} + \frac{1}{6}\sum_{i,j,h=0}^{m} \xi_i \xi_j \xi_h \mathcal{B}_{ijhk} + \mu_k[\lambda] - \lambda_b(\lambda - \frac{1}{2}\lambda_b)\sum_{i=0}^{m} \xi_i \mathcal{C}_{ik} = 0 \, , \quad k = 1 \ldots m \tag{1h}$$

Equation (1h) is an algebraic nonlinear system of m equations in the $m{+}1$ variables ξ_0, $\xi_1 \cdots \xi_m$, with known coefficients.

The software implementation of the asymptotic approach is quite easy and its computational cost remains of the order of that required by a standard linearized stability analysis [6]. Once the preprocessor phase of the analysis has been performed (steps i. to iv.), the presence of small load and geometrical imperfections can be taken into account in the post-processing phase (step v), by adding some, easily computed, additional imperfection terms in the expression of $\mu_k[\lambda]$, with a negligible computational cost, allowing for an inexpensive imperfection sensitivity analysis. From eq.(1h) we can also extract information about the worst imperfection shapes [20, 21] that we can use to improve the imperfection sensitivity analysis or for driving more detailed investigations through specialized path–following analysis [22].

2.2. Imperfection sensitivity analysis

The geometry and loads of thin-walled structures are affected by random distribution of small *imperfections*. In the proposed asymptotic method, the presence of small imperfections expressed

by a load $\tilde{p}[\lambda]$ and/or an initial displacement $\tilde{u}$ affect Eq.(1g) only on the imperfection term $\mu_k[\lambda]$ that becomes [6]

$$\mu_k[\lambda] = \frac{1}{2}\lambda_b(\lambda - \frac{1}{2}\lambda_b)\Phi_b'''\hat{u}^2\dot{v}_k + \frac{1}{6}\lambda_b^2(\lambda_b - 3\lambda)\Phi_b''''\hat{u}^3\dot{v}_k + \mu_k^g[\lambda] + \mu_k^l[\lambda] \tag{2}$$

with

$$\mu_k^g[\lambda] + \mu_k^l[\lambda] = \lambda\left(\Phi_c'''\hat{u}\tilde{u}\dot{v}_k - \tilde{p}[\lambda]\dot{v}_k\right) = \lambda\bar{\mu}_k \tag{3}$$

The aim of the *imperfection sensitivity analysis* is to link the presence of geometrical and load imperfections to the reduction of the limit load. For structures presenting coupled buckling modes, even a small load or geometrical imperfection may result in a marked reduction of the limit load with respect to the bifurcation load [23–28]. Therefore, an effective safety analysis should include an investigation of all possible imperfection shapes and sizes to recover the *worst case imperfection*.

The asymptotic approach provides a powerful tool for performing this extensive investigation. In fact, the analysis for a different imperfection only needs to update the imperfection factors $\mu_k^g[\lambda]$ and $\mu_k^l[\lambda]$ through Eq.(2)–(3) and solve the nonlinear system (1g)–(1h). Even if this system, which collects all the nonlinear parts of the original problem, proves to be highly nonlinear and some care has to be taken in treating the occurrence of multiple singularities, its solution through a path–following process is relatively easy because of the small number m of unknowns involved.

3. GEOMETRICALLY LINEAR FORMULATION

As it was stated earlier, the formulation must be capable of accurate representation of fourth-order terms on the potential energy. Therefore, we start with a mixed formulation. The initial reference configuration of the element is flat and referred to a local Cartesian frame $\{\boldsymbol{e}_1, \boldsymbol{e}_2, \boldsymbol{e}_3\}$. Furthermore, $\{x, y\}$ is a vector lying on the middle surface Ω defined by the unit vectors $\{\boldsymbol{e}_1, \boldsymbol{e}_2\}$, s is the thickness along the $\boldsymbol{e}_3$ direction, and Γ is the boundary of Ω. On this frame, the Hellinger-

Reissner strain energy for a flat shell can be written as

$$\Phi[\boldsymbol{t},\boldsymbol{d}] = \int_{\Omega} \left\{ \boldsymbol{t}^T \boldsymbol{D}\boldsymbol{d} - \frac{1}{2}\boldsymbol{t}^T \boldsymbol{E}^{-1}\boldsymbol{t} \right\} \mathrm{d}\Omega$$
$$\boldsymbol{t} = \begin{bmatrix} \boldsymbol{t}_m \\ \boldsymbol{t}_f \end{bmatrix}, \quad \boldsymbol{d} = \begin{bmatrix} \boldsymbol{d}_m \\ \boldsymbol{d}_f \end{bmatrix}, \quad \boldsymbol{D} = \begin{bmatrix} \boldsymbol{D}_m & \boldsymbol{0} \\ \boldsymbol{0} & \boldsymbol{D}_f \end{bmatrix} \tag{4}$$

where $\boldsymbol{t}_m, \boldsymbol{t}_f$ are the in- and out-of-plane stress parameters, respectively; and $\boldsymbol{d}_m, \boldsymbol{d}_f$ are the in- and out-plane kinematical parameters, defined as follows

$$\boldsymbol{t}_m = \begin{bmatrix} N_x \\ N_y \\ N_{xy} \end{bmatrix} \quad , \quad \boldsymbol{t}_f = \begin{bmatrix} M_x \\ M_y \\ M_{xy} \\ S_x \\ S_y \end{bmatrix} \quad , \quad \boldsymbol{d}_m = \begin{bmatrix} d_x \\ d_y \end{bmatrix} \quad , \quad \boldsymbol{d}_f = \begin{bmatrix} d_z \\ \varphi_x \\ \varphi_y \end{bmatrix} \tag{5}$$

where $\boldsymbol{N}, \boldsymbol{M}, \boldsymbol{S}$ are the membrane, bending, and shear stress resultants, respectively; and $\boldsymbol{d}, \boldsymbol{\varphi}$ are the midsurface strains and rotations, respectively.

Using first-order shear deformable theory (FSDT) [29], the differential operators $\boldsymbol{D}_m$ and $\boldsymbol{D}_f$ are defined as

$$\boldsymbol{D}_m = \begin{bmatrix} \partial/\partial x & 0 \\ 0 & \partial/\partial y \\ \partial/\partial y & \partial/\partial x \end{bmatrix} \quad , \quad \boldsymbol{D}_f = \begin{bmatrix} 0 & 0 & -\partial/\partial x \\ 0 & \partial/\partial y & 0 \\ 0 & \partial/\partial x & -\partial/\partial y \\ \partial/\partial x & 0 & 1 \\ \partial/\partial y & -1 & 0 \end{bmatrix} \tag{6}$$

The matrix of elastic coefficients, $\boldsymbol{E}$ can be written as and 8×8 matrix,

$$\boldsymbol{E} = \begin{bmatrix} \boldsymbol{E}_m & \boldsymbol{E}_{mf} \\ \boldsymbol{E}_{mf}^T & \boldsymbol{E}_f \end{bmatrix} \tag{7}$$

The definition of $\boldsymbol{E}_m, \boldsymbol{E}_f$ characterizing the membrane and flexural behaviour, respectively, and that of $\boldsymbol{E}_{mf}$ containing the membrane/flexural coupling are computed in terms of the lamina material properties and the laminate stacking sequence (LSS) as described by equation (6.16) in

[30]. When the stress resultants are defined so that the equilibrium equations are satisfied with zero load, the following identity holds [31]

$$\int_{\Omega} \boldsymbol{t}^T \boldsymbol{D}\boldsymbol{d}\,\mathrm{d}\Omega = \int_{\Gamma} \boldsymbol{t}^T \boldsymbol{N}^T \boldsymbol{d}\,\mathrm{d}\Gamma = \int_{\Gamma} \boldsymbol{t}_m^T \boldsymbol{N}_m^T \boldsymbol{d}_m\,\mathrm{d}\Gamma + \int_{\Gamma} \boldsymbol{t}_f^T \boldsymbol{N}_f^T \boldsymbol{d}_f\,\mathrm{d}\Gamma \tag{8}$$

where $\boldsymbol{N}$ is the matrix collecting the components of the unit outward normal to the contour Γ, that can be split into membrane $\boldsymbol{N}_m$ and bending $\boldsymbol{N}_f$ parts

$$\boldsymbol{N} = \begin{bmatrix} \boldsymbol{N}_m & \boldsymbol{0} \\ \boldsymbol{0} & \boldsymbol{N}_f \end{bmatrix} \tag{9}$$

3.1. Mixed finite element

Assuming a mixed interpolation for the stress resultants and displacements, a discrete expression for the Hellinger–Reissner mixed strain energy (4) can be evaluated. In general, the mixed interpolation can be written as

$$\boldsymbol{t} = \boldsymbol{B}\boldsymbol{t}_e \quad , \quad \boldsymbol{d} = \boldsymbol{U}\boldsymbol{d}_e \tag{10}$$

where $\boldsymbol{B}$ is the matrix collecting the assumed stress modes, $\boldsymbol{t}_e$ is the vector of stress parameters, $\boldsymbol{U}$ is the matrix of the displacement shape functions and $\boldsymbol{d}_e$ is the vector of displacement and rotation kinematical parameters. Substituting (10) into (4) and integrating on the element domain Ω_e leads to the evaluation of the element mixed energy

$$\Phi_e[\boldsymbol{t}_e, \boldsymbol{d}_e] = \boldsymbol{t}_e^T \boldsymbol{D}_e \boldsymbol{d}_e - \frac{1}{2} \boldsymbol{t}_e^T \boldsymbol{H}_e \boldsymbol{t}_e \quad , \quad \begin{cases} \boldsymbol{D}_e = \displaystyle\int_{\Omega_e} \left\{ \boldsymbol{B}^T \boldsymbol{D}\boldsymbol{U} \right\} \mathrm{d}\Omega \\ \boldsymbol{H}_e = \displaystyle\int_{\Omega_e} \left\{ \boldsymbol{B}^T \boldsymbol{E}^{-1} \boldsymbol{B} \right\} \mathrm{d}\Omega \end{cases} \tag{11}$$

where $\boldsymbol{D}_e$ and $\boldsymbol{H}_e$ are the compatibility and flexibility matrices, respectively [32].

When the assumed stress modes (shape functions) are chosen so that the stress resultants identically satisfy equilibrium equations with zero load (self equilibrating stress field in the element), the compatibility matrix can be evaluated on the element contour Γ_e, i.e., Eq. (8) yields

$$\boldsymbol{D}_e = \int_{\Gamma_e} \boldsymbol{B}^T \boldsymbol{N}^T \boldsymbol{U}\,\mathrm{d}\Gamma \tag{12}$$

Applying static condensation to the stress parameters $\boldsymbol{t}_e$, the element energy can be evaluated solely in terms of kinematic parameters $\boldsymbol{d}_e$, and using (12), the displacements and rotations (26),(31), need to be interpolated only along the contour. Details of the element implementation are given in §5.

4. GEOMETRICALLY NON LINEAR FORMULATION

A linear finite element can be made geometrically nonlinear using corotational algebra to describe the rigid body motion [8]. Following the original proposal by Rankin et. al [33, 34], this framework is still used [35–40]. With respect to the fixed frame $\{\boldsymbol{e}_1, \boldsymbol{e}_2, \boldsymbol{e}_3\}$, a corotational (CR) frame $\{\bar{\boldsymbol{e}}_1, \bar{\boldsymbol{e}}_2, \bar{\boldsymbol{e}}_3\}$ is defined as

$$\bar{\boldsymbol{e}}_k = \boldsymbol{Q}[\boldsymbol{\alpha}]\boldsymbol{e}_k, \quad k = 1..3 \tag{13}$$

with $\boldsymbol{Q}$ being a rigid rotation, parametrized by the rotation vector $\boldsymbol{\alpha}$ according to Rodrigues' formulation [41] (see Fig. 1) . The origin is assumed to be translated by vector $\boldsymbol{c}$. Denoting by $\boldsymbol{d}$ and $\boldsymbol{R}$ the displacement and the rotation associated to position $\boldsymbol{X}$ in the fixed reference frame, the following geometrical relationships hold

$$\bar{\boldsymbol{d}} = \boldsymbol{Q}^T(\boldsymbol{X} + \boldsymbol{d} - \boldsymbol{c}) - \boldsymbol{X} \quad , \quad \bar{\boldsymbol{R}} = \boldsymbol{Q}^T\boldsymbol{R} \tag{14}$$

with $\bar{\boldsymbol{d}}$ and $\bar{\boldsymbol{R}}$ being the displacement and the rotation in the corotational frame. Using a vector parametrization for $\bar{\boldsymbol{R}}$ and $\boldsymbol{R}$ and denoting by $\bar{\boldsymbol{\psi}}$ and $\boldsymbol{\psi}$ the rotation vectors, we have

$$\bar{\boldsymbol{\psi}} = \log(\bar{\boldsymbol{R}}[\bar{\boldsymbol{\psi}}]) = \log\left(\boldsymbol{Q}^T[\boldsymbol{\alpha}]\boldsymbol{R}[\boldsymbol{\psi}]\right) \tag{15}$$

A CR frame can be defined for each element through the element rotation vector $\boldsymbol{\alpha}_e$ which is a function of the element kinematical parameters $\boldsymbol{d}_e$ in the fixed frame

$$\boldsymbol{\alpha}_e = \boldsymbol{\alpha}_e[\boldsymbol{d}_e] \tag{16}$$

The local kinematical parameters $\bar{\boldsymbol{d}}_e$ in the CR frame are related to $\boldsymbol{d}_e$ by the geometrical transfor-

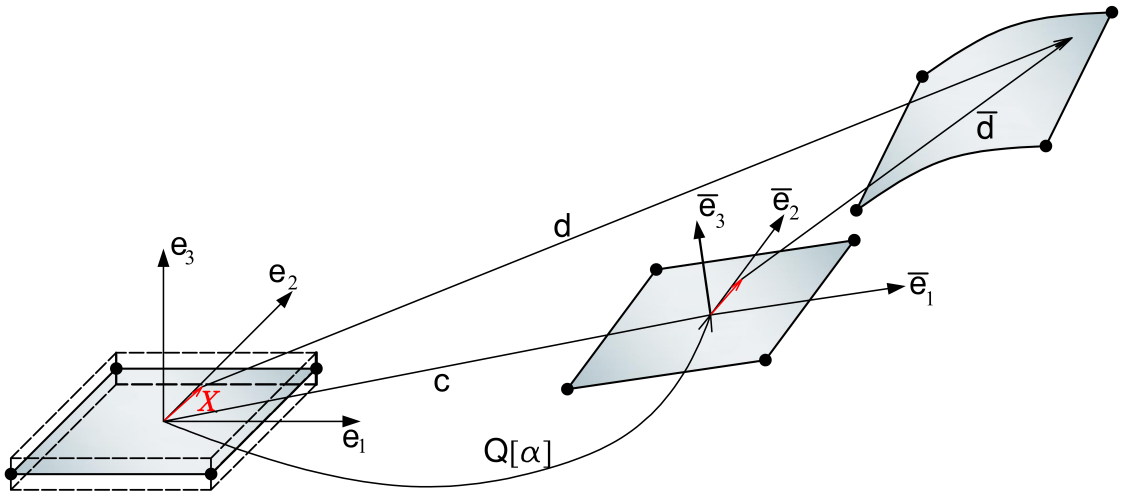

Figure 1: Corotational frame.

mation

$$\bar{\boldsymbol{d}}_e = \boldsymbol{g}[\boldsymbol{d}_e] \tag{17}$$

where $\boldsymbol{g}$ collects the CR transformations for displacements (14) and rotations (15) opportunely rearranged in terms of the local kinematical parameters $\bar{\boldsymbol{d}}_e$ of the finite element, as it is done in (35). See [9] for further details.

Based on the above relations, the linear finite element characterized by energy (11) can be transformed into a geometrically nonlinear element simply by introducing a corotational description and assuming that the element kinematical parameters in eq. (11) are referred to the corotational frame. This leads to:

$$\Phi_e[\boldsymbol{t}_e, \boldsymbol{d}_e] = \boldsymbol{t}_e^T \boldsymbol{D}_e \boldsymbol{g}[\boldsymbol{d}_e] - \frac{1}{2}\boldsymbol{t}_e^T \boldsymbol{H}_e \boldsymbol{t}_e \tag{18}$$

The element energy can be expressed in terms of the element vector

$$\boldsymbol{u}_e = \{\boldsymbol{t}_e,\, \boldsymbol{d}_e\}^T \tag{19}$$

which collects all the parameters defining the element configuration in a single vector and can be related to the global configuration vector $\boldsymbol{u}$ through the standard assemblage procedure

$$\boldsymbol{u}_e = \boldsymbol{A}_e \boldsymbol{u} \tag{20}$$

where the matrix $\boldsymbol{A}_e$ implicitly contains the compatibility constraints between elements. For the Hellinger-Reissner formulation used here, the components of $\boldsymbol{u}$ are the global displacements/rotations of the nodes of the elements and the the stress parameters of each element. Using static condensation, the stress parameters can be eliminated at the element level, and then a compatible scheme can be employed [42].

5. ELEMENT IMPLEMENTATION

The mixed isostatic self-equilibrated flat shell element MISS-4 [10, 14] is used as the starting point here. It is a 4–node quadrilateral externally defined by 24 kinematical dofs and internally by an isostatic self–equilibrated stress expansion represented by 18 parameters.

The local reference frame is a Cartesian frame $\{\boldsymbol{e}_1, \boldsymbol{e}_2, \boldsymbol{e}_3\}$ defined so that the average Jacobian of the iso–parametric transformation is symmetric. For each side Γ_k, connecting nodes i and j in counterclockwise order, we define Ξ_k, Δ_k and its external normal $\boldsymbol{n}_k$ according to the following expressions

$$\begin{aligned}
\Xi_k &= \begin{bmatrix} \Xi_{kx} \\ \Xi_{ky} \end{bmatrix} = \begin{bmatrix} x_j + x_i \\ y_j + y_i \end{bmatrix} \\
\Delta_k &= \begin{bmatrix} \Delta_{kx} \\ \Delta_{ky} \end{bmatrix} = \begin{bmatrix} x_j - x_i \\ y_j - y_i \end{bmatrix} \\
\boldsymbol{n}_k &= \begin{bmatrix} n_{kx} \\ n_{ky} \end{bmatrix} = \frac{1}{L_k} \begin{bmatrix} \Delta_{ky} \\ -\Delta_{kx} \end{bmatrix}
\end{aligned} \tag{21}$$

with $L_k = \sqrt{\Delta_{kx}^2 + \Delta_{ky}^2}$ being the side length. The one–dimensional abscissa $-1 \le \zeta \le 1$ along Γ_k is defined as

$$x = \frac{1}{2}(\Xi_{kx} + \Delta_{kx}\,\zeta) \quad , \quad y = \frac{1}{2}(\Xi_{ky} + \Delta_{ky}\,\zeta) \tag{22}$$

The membrane and bending stress modes are assumed to be uncoupled and the stress resultants approximation is written as

$$\begin{bmatrix} \boldsymbol{t}_m \\ \boldsymbol{t}_f \end{bmatrix} = \begin{bmatrix} \boldsymbol{B}_m & \boldsymbol{0} \\ \boldsymbol{0} & \boldsymbol{B}_f \end{bmatrix} \begin{bmatrix} \boldsymbol{\beta}_m \\ \boldsymbol{\beta}_f \end{bmatrix} \tag{23}$$

with $\boldsymbol{B}_m, \boldsymbol{B}_f$ are the matrices collecting the approximating functions for the membrane and flexural part, respectively, and $\boldsymbol{\beta}_m, \boldsymbol{\beta}_f$ are the corresponding stress parameters.

The membrane behavior of MISS-4 is represented by 9 stress parameters

$$\boldsymbol{B}_m = \begin{bmatrix} 1 & 0 & 0 & y & 0 & x & 0 & y^2 & -2\,a^2 xy \\ 0 & 1 & 0 & 0 & x & 0 & y & -x^2 & 2\,b^2 xy \\ 0 & 0 & 1 & 0 & 0 & -y & -x & 0 & a^2 y^2 - b^2 x^2 \end{bmatrix} \tag{24}$$

where a and b are the diagonal coefficients of the Jacobian matrix of the iso-parametric transformation [15].

The flexural stress resultants are described using 9 stress parameters

$$\boldsymbol{B}_f = \begin{bmatrix} 1 & 0 & 0 & x & 0 & y & 0 & x\,y & 0 \\ 0 & 1 & 0 & 0 & x & 0 & y & 0 & x\,y \\ 0 & 0 & 1 & 0 & y\,\bar{c} & x/\bar{c} & 0 & 0 & 0 \\ 0 & 0 & 0 & -1 & -\bar{c} & 0 & 0 & -y & 0 \\ 0 & 0 & 0 & 0 & 0 & -1/\bar{c} & -1 & 0 & -x \end{bmatrix} \tag{25}$$

where $\bar{c} = a^2/b^2$. The form of (24)–(25) are chosen so that the stress resultant approximation (23) is self-equilibrated and isostatic [15, 42]. Really, the stress resultants interpolation is represented by 18 parameters corresponding to deformation modes of the elements (24 kinematic parameters minus 6 rigid body motion).

The interpolation of displacements and rotations is based on a 4-node element with 6 degrees of freedom (dof) per node. Recalling that the stress satisfies the equilibrium equation, the internal work can be obtained by integration along the element contour and, therefore, displacements and rotations need to be defined solely on the element boundary. The displacement interpolation along each side is defined as the sum of three terms as follows

$$\bar{\boldsymbol{d}}_k[\zeta] = \bar{\boldsymbol{d}}_{kl}[\zeta] + \bar{\boldsymbol{d}}_{kq}[\zeta] + \bar{\boldsymbol{d}}_{kc}[\zeta] \tag{26}$$

The first term is a linear expansion

$$\bar{\boldsymbol{d}}_{kl}[\zeta] = \frac{1}{2}[(1-\zeta)\bar{\boldsymbol{d}}^{(i)} + (1+\zeta)\bar{\boldsymbol{d}}^{(j)}] \quad \text{with} \quad \begin{cases} \bar{\boldsymbol{d}}^{(i)} = [\bar{d}_x^{(i)},\, \bar{d}_y^{(i)},\, \bar{d}_z^{(i)}]^T \\ \bar{\boldsymbol{d}}^{(j)} = [\bar{d}_x^{(j)},\, \bar{d}_y^{(j)},\, \bar{d}_z^{(j)}]^T \end{cases} \tag{27}$$

where i and j denote the nodes of side k. The second and third terms correspond to a quadratic and a cubic expansion for the normal component of the side displacement

$$\begin{cases} \bar{\boldsymbol{d}}_{kq}[\zeta] = \dfrac{1}{8}\, L_k(\zeta^2-1) \begin{bmatrix} (\bar{\varphi}_z^{(i)} - \bar{\varphi}_z^{(j)})\, \boldsymbol{n}_k \\ -(\bar{\boldsymbol{\varphi}}^{(i)} - \bar{\boldsymbol{\varphi}}^{(j)})^T \boldsymbol{n}_k \end{bmatrix} \\ \bar{\boldsymbol{d}}_{kc}[\zeta] = \dfrac{1}{4}\, L_k \zeta(1-\zeta^2) \begin{bmatrix} \boldsymbol{n}_k \\ 0 \end{bmatrix} \bar{\alpha} \end{cases} \quad \text{with} \quad \begin{cases} \bar{\boldsymbol{\varphi}}^{(i)} = [\bar{\varphi}_x^{(i)},\, \bar{\varphi}_y^{(i)}]^T \\ \bar{\boldsymbol{\varphi}}^{(j)} = [\bar{\varphi}_x^{(j)},\, \bar{\varphi}_y^{(j)}]^T \end{cases} \tag{28}$$

The parameter $\bar{\alpha}$ in the cubic term is taken as the average distortional in–plane nodal rotation

$$\bar{\alpha} = \frac{1}{4}\sum_{i=1}^{4} \bar{\varphi}_z^{(i)} - \bar{\varphi}_z \tag{29}$$

where $\bar{\varphi}_z$ is the average in–plane rigid rotation of the element

$$\bar{\varphi}_z = \boldsymbol{N}_\alpha \bar{\boldsymbol{d}}_{me}, \quad \boldsymbol{N}_\alpha = \frac{1}{4\Omega_e}\,[-\Delta_{4y},\, \Delta_{4x},\, -\Delta_{1y},\, \Delta_{1x},\, -\Delta_{2y},\, \Delta_{2x},\, -\Delta_{3y},\, \Delta_{3x}\,] \tag{30}$$

where $\bar{\boldsymbol{d}}_{me}$ is 12-component vector collecting the kinematical parameters that represent the membrane behavior of the element, i.e., $\bar{d}_x^{(i)}$, $\bar{d}_y^{(i)}$, $\bar{\varphi}_z^{(i)}$.

Finally, a simple bilinear interpolation is assumed for bending rotations along the edge [31]

$$\bar{\boldsymbol{\varphi}}_k[\zeta] = \frac{1}{2}\,[(1-\zeta)\bar{\boldsymbol{\varphi}}^{(i)} + (1+\zeta)\bar{\boldsymbol{\varphi}}^{(j)}] \tag{31}$$

The corotational frame is obtained by simply setting the rotation vector equal to the average nodal rotations in the fixed frame

$$\boldsymbol{\alpha}_e = \frac{1}{4}\sum_{i=1}^{4} \boldsymbol{\varphi}^{(i)} \tag{32}$$

and setting the translation $\boldsymbol{c}_e$ (see eq. (14)) as

$$\boldsymbol{c}_e = \frac{1}{4}\sum_{i=1}^{4} \boldsymbol{d}^{(i)} \tag{33}$$

The choice about $\boldsymbol{\alpha}_e$ offers a good compromise between accuracy and simplicity in the evaluation of high order energy variations for asymptotic analysis [8]. The choice (32) allows the geometrical transformation law to be defined as (17). Really, we have

$$\bar{\boldsymbol{d}}_e = \begin{bmatrix} \bar{\boldsymbol{d}}_e^{(1)} \\ \bar{\boldsymbol{d}}_e^{(2)} \\ \bar{\boldsymbol{d}}_e^{(3)} \\ \bar{\boldsymbol{d}}_e^{(4)} \end{bmatrix} \quad , \quad \bar{\boldsymbol{d}}_e^{i} = \begin{bmatrix} \bar{\boldsymbol{d}}^{(i)} \\ \bar{\boldsymbol{\varphi}}^{(i)} \end{bmatrix} \tag{34}$$

and finally using eqs. (14) and (15)

$$\boldsymbol{d}_e^i = \begin{bmatrix} \boldsymbol{Q}^T[\boldsymbol{\alpha}_e](\boldsymbol{X}^i + \boldsymbol{d}_e^i - \boldsymbol{c}_e) - \boldsymbol{X}^i \\ \log\left(\boldsymbol{Q}^T[\boldsymbol{\alpha}_e]\boldsymbol{R}[\boldsymbol{\varphi}^i]\right) \end{bmatrix} \tag{35}$$

6. KOITER ASYMPTOTIC FINITE ELEMENT ANALYSIS

To apply the asymptotic approach to the corotational version of element MISS-4, explicit expressions for the second-, third- and fourth–order energy variations need to be computed [8] with respect to a configuration that can be either the initial ($\boldsymbol{u}_0$ in (1a)) or the bifurcation one ($\boldsymbol{u}_0 + \lambda\hat{\boldsymbol{u}}$ in (1a)). For computation of second or higher order terms, the constant terms $\boldsymbol{u}_0$ and $\boldsymbol{u}_0 + \lambda\hat{\boldsymbol{u}}$ are irrelevant, so at the element level we can assume $\boldsymbol{d}_e = \boldsymbol{0}$.

The corotational approach is very convenient to express the strain energy variations, because the only nonlinearity is limited to the geometrical relationship $\boldsymbol{g}[\boldsymbol{d}_e]$, eq. (17). The Taylor expansion of this relationship can be written as

$$\boldsymbol{g}[\boldsymbol{d}_e] = \boldsymbol{g}_1[\boldsymbol{d}_e] + \frac{1}{2}\boldsymbol{g}_2[\boldsymbol{d}_e, \boldsymbol{d}_e] + \frac{1}{6}\boldsymbol{g}_3[\boldsymbol{d}_e, \boldsymbol{d}_e, \boldsymbol{d}_e] + \frac{1}{24}\boldsymbol{g}_4[\boldsymbol{d}_e, \boldsymbol{d}_e, \boldsymbol{d}_e, \boldsymbol{d}_e] + \cdots \tag{36}$$

where $\boldsymbol{g}_n$ are n–multilinear symmetric forms which express the nth Fréchet variations of function $\boldsymbol{g}[\boldsymbol{d}_e]$. In the following, the vector $\boldsymbol{u}_i$ ($i = 1 \ldots 4$) denotes a generic variation of the global finite ele-

ment configuration vector and the vector $\boldsymbol{u}_{ei} = \boldsymbol{A}_e \boldsymbol{u}_i = \{\boldsymbol{t}_{ei}, \boldsymbol{d}_{ei}\}^T$ denotes the corresponding vector at the element level, that collects stress and displacement parameters. With the same notation, $\boldsymbol{u}_0$ and $\boldsymbol{u}_{e0}$ are the global and element reference configuration vectors.

6.1. Second-order variations

Second–order energy variations are used in the evaluation of the fundamental path (1a) and the buckling modes $\dot{\boldsymbol{v}}$. In both cases, using expansion (36) and the energy expression (18), the contribution of the element to the energy variation can be expressed as

$$\Phi_e^{''} \boldsymbol{u}_{e1} \boldsymbol{u}_{e2} = \boldsymbol{t}_{e1}^T \boldsymbol{D}_e \boldsymbol{g}_1[\boldsymbol{d}_{e2}] + \boldsymbol{t}_{e2}^T \boldsymbol{D}_e \boldsymbol{g}_1[\boldsymbol{d}_{e1}] - \boldsymbol{t}_{e1}^T \boldsymbol{H}_e \boldsymbol{t}_{e2} + \boldsymbol{t}_{e0}^T \boldsymbol{D}_e \boldsymbol{g}_2[\boldsymbol{d}_{e1}, \boldsymbol{d}_{e2}] \tag{37}$$

Introducing matrices $\boldsymbol{L}_1$ and $\boldsymbol{G}[\boldsymbol{t}_e]$ through the following equivalences

$$\boldsymbol{L}_1 \boldsymbol{d}_{ej} = \boldsymbol{g}_1[\boldsymbol{d}_{ej}] \quad , \quad \boldsymbol{d}_{e1}^T \boldsymbol{G}[\boldsymbol{t}_{e0}] \boldsymbol{d}_{e2} = \boldsymbol{t}_{e0}^T \boldsymbol{D}_e \boldsymbol{g}_2[\boldsymbol{d}_{e1}, \boldsymbol{d}_{e2}], \tag{38}$$

eq. (37) can be rearranged in a more compact form:

$$\boldsymbol{u}_{e1}^T \Phi_e^{''} \boldsymbol{u}_{e2} = \boldsymbol{u}_{e1}^T \boldsymbol{K}_e \boldsymbol{u}_{e2} \quad , \quad \boldsymbol{K}_e = \begin{bmatrix} -\boldsymbol{H}_e & \boldsymbol{D}_e \boldsymbol{L}_1 \\ \boldsymbol{L}_1^T \boldsymbol{D}_e^T & \boldsymbol{G}[\boldsymbol{t}_{e0}] \end{bmatrix} \tag{39}$$

The mixed tangent matrix of the element $\boldsymbol{K}_e$ can be directly used, through a standard assemblage process, to obtain the overall stiffness matrix $\boldsymbol{K}$

$$\boldsymbol{u}_1^T \Phi^{''} \boldsymbol{u}_2 = \boldsymbol{u}_1^T \boldsymbol{K} \boldsymbol{u}_2 \quad , \quad \boldsymbol{K} = \sum_e \boldsymbol{A}_e^T \boldsymbol{K}_e \boldsymbol{A}_e \tag{40}$$

6.2. Third-order variations

Third-order energy variations are used in Koiter analysis to evaluate the third–order coefficients and are also used to evaluate the secondary force vectors. The element contribution to the scalar coefficients can be easily calculated using the general formula

$$\begin{aligned} \Phi_e^{'''} \boldsymbol{u}_{e1} \boldsymbol{u}_{e2} \boldsymbol{u}_{e3} = {} & \boldsymbol{t}_{e1}^T \boldsymbol{D}_e \boldsymbol{g}_2[\boldsymbol{d}_{e2}, \boldsymbol{d}_{e3}] + \boldsymbol{t}_{e2}^T \boldsymbol{D}_e \boldsymbol{g}_2[\boldsymbol{d}_{e3}, \boldsymbol{d}_{e1}] + \boldsymbol{t}_{e3}^T \boldsymbol{D}_e \boldsymbol{g}_2[\boldsymbol{d}_{e1}, \boldsymbol{d}_{e2}] \\ & + \boldsymbol{t}_{e0}^T \boldsymbol{D}_e \boldsymbol{g}_3[\boldsymbol{d}_{e1}, \boldsymbol{d}_{e2}, \boldsymbol{d}_{e3}] \end{aligned} \tag{41}$$

Then the element contributions can be simply added to get the global values. On the other hand, taking advantage of the above expression, the element contribution to vector secondary force vector can be evaluated by

$$\Phi_e'''\boldsymbol{u}_{e1}\boldsymbol{u}_{e2} = \boldsymbol{p}_e = \begin{bmatrix} \boldsymbol{D}_e\boldsymbol{g}_2[\boldsymbol{d}_{e1},\boldsymbol{d}_{e2}] \\ \boldsymbol{G}[\boldsymbol{t}_{e1}]\boldsymbol{d}_{e2} + \boldsymbol{G}[\boldsymbol{t}_{e2}]\boldsymbol{d}_{e1} + \boldsymbol{q}[\boldsymbol{t}_{e0},\boldsymbol{d}_{e1},\boldsymbol{d}_{e2}] \end{bmatrix} \tag{42}$$

where vector $\boldsymbol{q}$ is defined according to the following condition:

$$\boldsymbol{d}_{e3}^T\boldsymbol{q}[\boldsymbol{t}_{e0},\boldsymbol{d}_{e1},\boldsymbol{d}_{e2}] = \boldsymbol{t}_{e0}^T\boldsymbol{D}_e\boldsymbol{g}_3[\boldsymbol{d}_{e1},\boldsymbol{d}_{e2},\boldsymbol{d}_{e3}] \tag{43}$$

Then, the overall vector is obtained by standard assemblage

$$\Phi'''\boldsymbol{u}_1\boldsymbol{u}_2 = \sum_e \boldsymbol{A}_e^T\boldsymbol{p}_e[\boldsymbol{u}_{e1},\boldsymbol{u}_{e2}]$$

6.3. Fourth-order variations

Finally, fourth-order energy variations, used to evaluate the fourth–order coefficients, can be computed by summing the relevant element contributions based on the following expression

$$\begin{aligned} \Phi_e''''\boldsymbol{u}_{e1}\boldsymbol{u}_{e2}\boldsymbol{u}_{e3}\boldsymbol{u}_{e4} = {} & \boldsymbol{t}_{e1}^T\boldsymbol{D}_e\boldsymbol{g}_3[\boldsymbol{d}_{e2},\boldsymbol{d}_{e3},\boldsymbol{d}_{e4}] + \boldsymbol{t}_{e2}^T\boldsymbol{D}_e\boldsymbol{g}_3[\boldsymbol{d}_{e3},\boldsymbol{d}_{e4},\boldsymbol{d}_{e1}] \\ & + \boldsymbol{t}_{e3}^T\boldsymbol{D}_e\boldsymbol{g}_3[\boldsymbol{d}_{e4},\boldsymbol{d}_{e1},\boldsymbol{d}_{e2}] + \boldsymbol{t}_{e4}^T\boldsymbol{D}_e\boldsymbol{g}_3[\boldsymbol{d}_{e1},\boldsymbol{d}_{e2},\boldsymbol{d}_{e3}] \\ & + \boldsymbol{t}_{e0}^T\boldsymbol{D}_e\boldsymbol{g}_4[\boldsymbol{d}_{e1},\boldsymbol{d}_{e2},\boldsymbol{d}_{e3},\boldsymbol{d}_{e4}] \end{aligned} \tag{44}$$

7. NUMERICAL RESULTS

In this section, the proposed methodology for the evaluation of imperfection sensitivity is applied first to a folded plate structure, and then to cylindrical shells that are know to be imperfection sensitive.

7.1. Imperfection sensitivity analysis of a hinged box in compression

To illustrate some of the capabilities of the proposed element, the box shown in Figure 2 is analyzed. The geometrical data are $L = 1000$ mm, $a = 500$ mm. Three witdh/thickness ratios are considered: $a/t = 1/500$, $1/400$, $3/1000$. The ply properties are $E_1 = 123.55$ GPa; $E_2 = 8.708$

GPa; $G = 5.695$ GPa; $\nu_{12} = 0.32$. The laminate stacking sequence is $[0/0/19/-19/37/-37/45/-45/51/-51]$. The bottom end of the box is hinged. The load is a uniform edge pressure applied at the top end of the box.

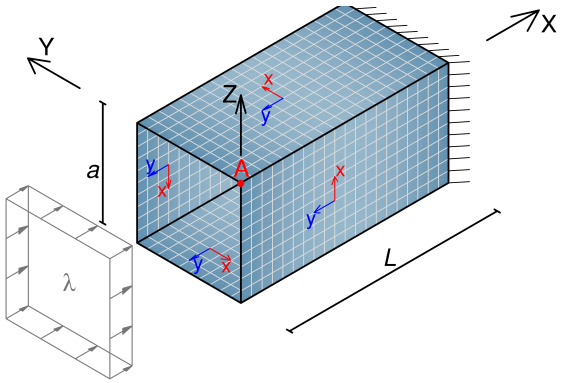

Figure 2: Geometry, boundary conditions, and load for the box in compression.

7.1.1. Buckling analysis

Once the fundamental path is evaluated (eq. 1a), a buckling analysis (eq. 1c) is performed. The first eight buckling loads are reported in Table 1 for different values of width/thickness ratio. The buckling modes for $t/a = 1/400$ are shown in Figure 3. The buckling modes are then used to generate random geometrical imperfections.

t/a	λ_1	λ_2	λ_3	λ_4	λ_5	λ_6	λ_7	λ_8
1/500	608.28	760.38	760.38	920.14	1005.10	1102.10	1281.22	1281.22
1/400	1187.16	1484.52	1484.52	1796.78	1961.72	2151.00	2501.40	2501.40
3/1000	2049.80	2564.00	2564.00	3104.00	3387.40	3714.20	4319.40	4319.40

Table 1: Buckling loads (in Newtons) for the box in compression at several t/a ratios.

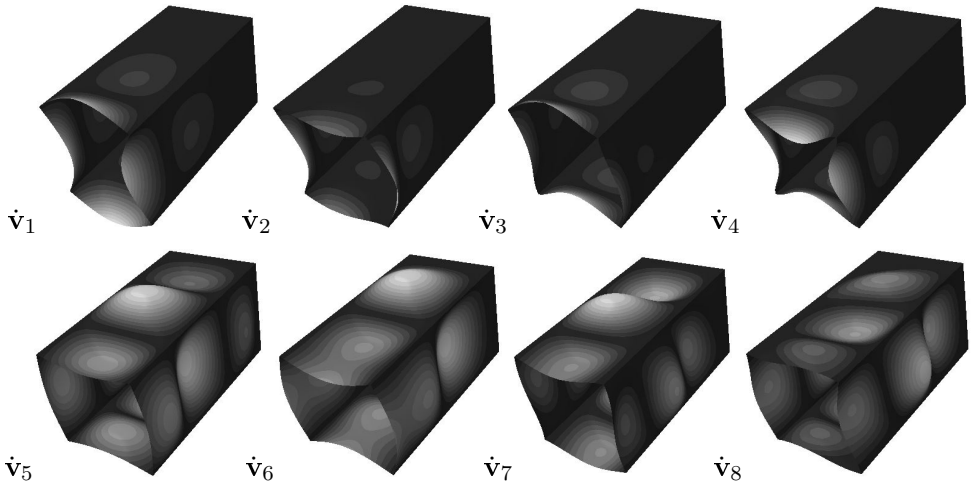

Figure 3: Buckling modes for the box in compression at $t/a = 1/400$.

7.1.2. Post-buckling and imperfection sensitivity analysis

Some of the quadratic corrections (eq.1d) are shown in Figure (4) and used to recover the structural behaviour of the imperfect structure. Only geometrical imperfections $\tilde{u}$ have been considered. In particular, they are generated as linear combinations of the buckling modes $\dot{v}_i$, that is

$$\tilde{u} = \sum_{i}^{m} r_i \dot{v}_i \tag{45}$$

where r_i are random numbers, and m is the number buckling modes included in the expansion (1e). For this example, $m = 8$ is used. Note that our aim is to find the worst imperfection. Then, the real shape of the imperfection is not required and only the linear combinations of buckling modes are considered. The maximum value of $\tilde{u}_{max}$ is assumed to be bound by a tolerance

$$\tilde{u}_{max}/t \leq tol \tag{46}$$

For this example, $\tilde{u}_{max}/t = 1.5$ is used, while in practice the amplitude of the imperfection depends on the manufacturing process. Obviously, the amplitude of the imperfection affects the results in term of limit loads, as shown in the following.

The equilibrium paths for 500 random geometrical imperfections have been graphed in Figure (5) in terms of mode amplitude $\xi_i, i = 1..8$, and in Figure (6) in terms of nodal displacements. Loss of stability in the post-critical range and the presence of attractive paths [20, 22] can be seen in the figures. Even if the random imperfections generate different behaviour within a range, the imperfect paths manifest a convergent behaviour to some particular paths (i.e. attractive paths). This is also clear in Figure 7, where the interaction between the first mode and the remaining seven modes are shown, as well as in Figure 8 in terms of deformed configurations. A-priori knowledge of attractive paths could be used to increase the efficiency of the Monte Carlo simulation, by reducing the space of trial imperfections.

Monte Carlo simulation allows us to evaluate the frequency of occurrence of limit load (Figure 9), the worst imperfection (Figure 10), and the shape of the structure at the minimum limit load (Figure 11).

Finally, to show the sensitivity of the structure to the worst imperfection magnitude $\tilde{u}_w$, further

sensitivity analysis has been performed varying $\tilde{u}_{max}/t$. The results are shown in Figure 12, showing that this composite box is very sensitive to imperfections.

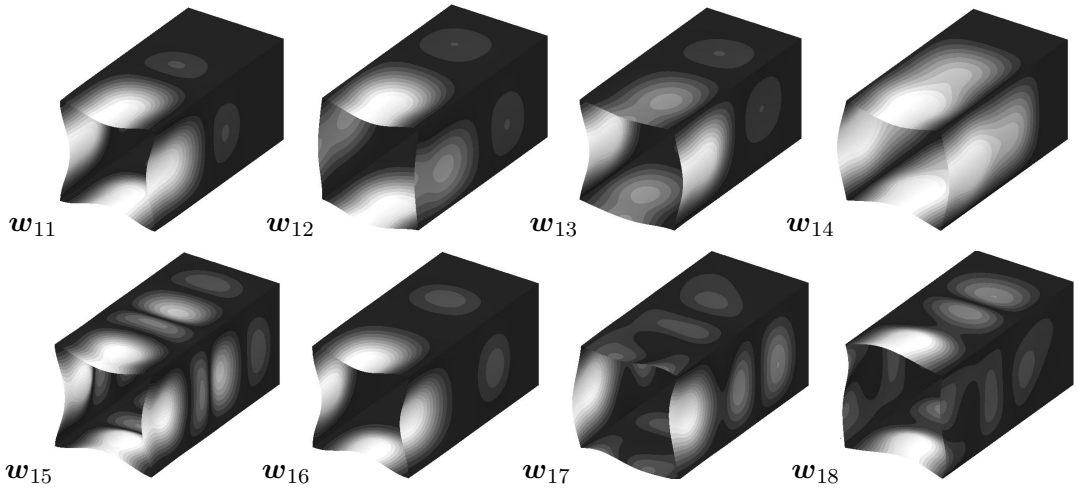

Figure 4: Quadratic corrections for the box in compression, with $t/a = 1/400$.

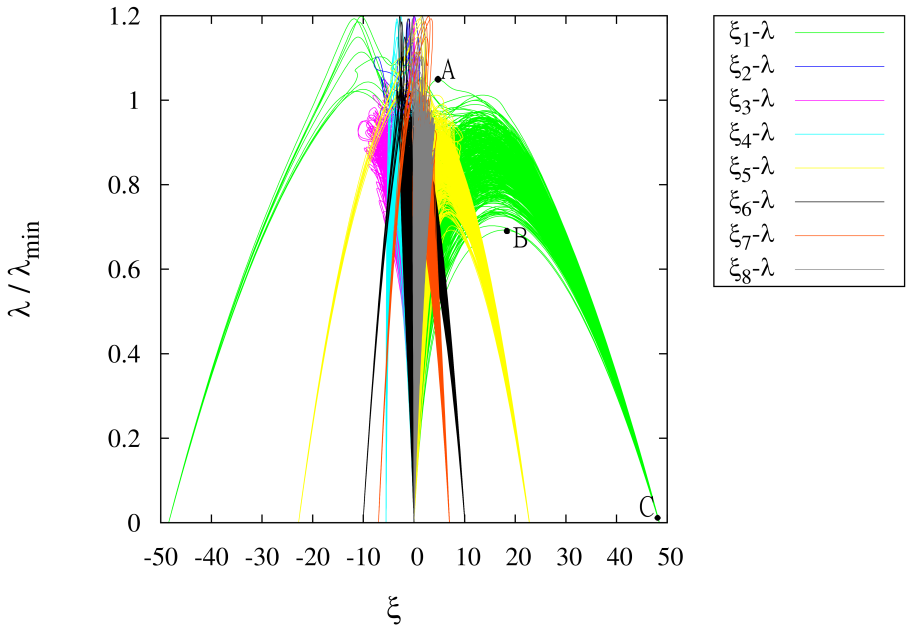

Figure 5: Equilibrium paths λ versus ξ_i, $i = 1...8$ for the box in compression, with $t/a = 1/400$.

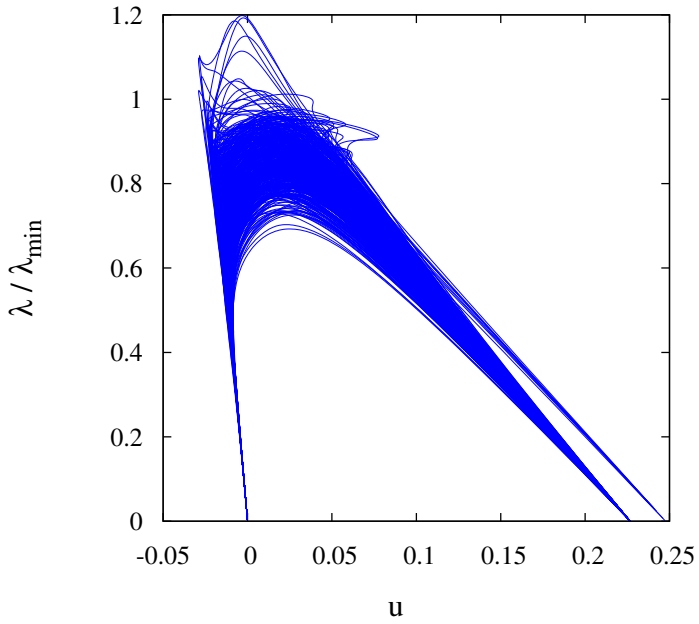

Figure 6: Equilibrium paths λ versus u for the box in compression, with $t/a = 1/400$. The displacement component u_x is measured at point A in Fig.(2).

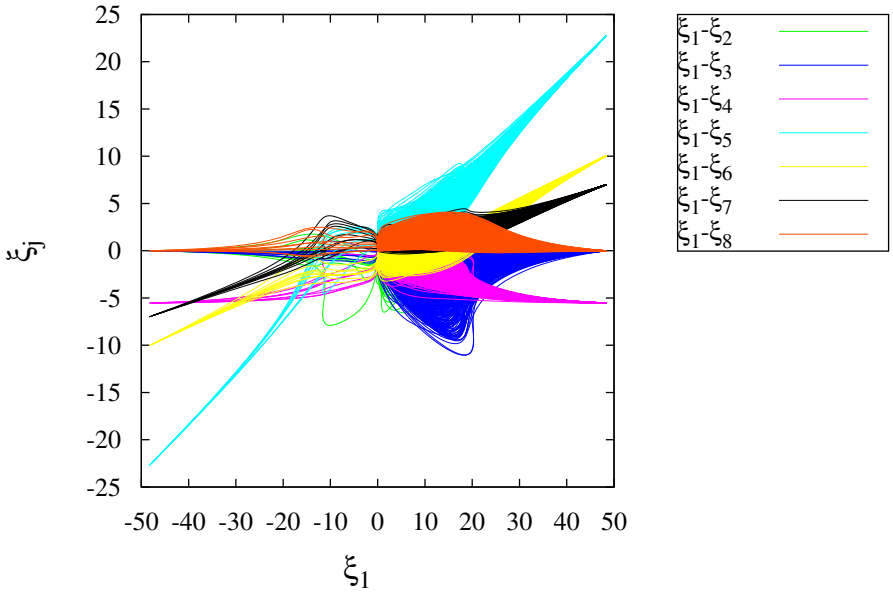

Figure 7: Interaction between the first mode (with amplitude ξ_1) and the remaining modes $\xi_j, j = 2..8$. The presence of attractive paths is clear.

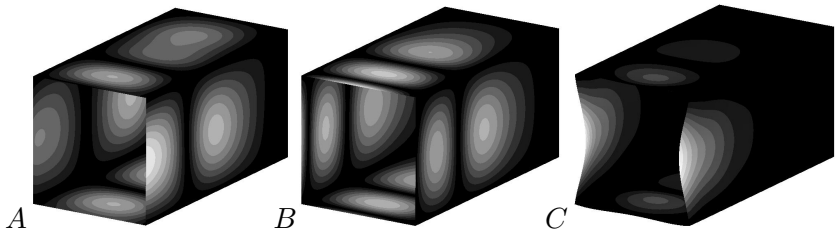

Figure 8: Deformed configuration at points A, B and C, labeled in Figure (5).

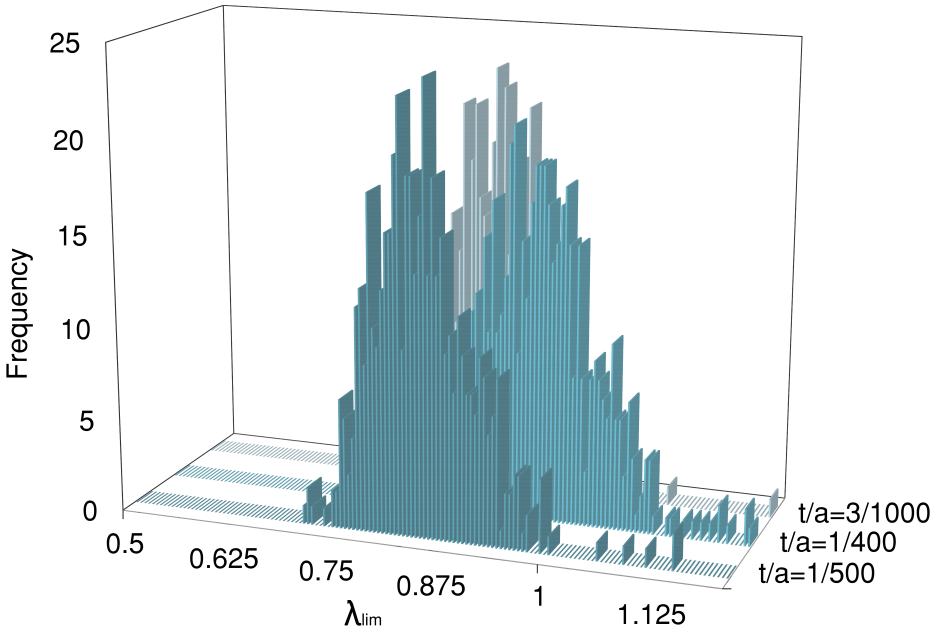

Figure 9: Frequency distribution of the lowest limit load found λ_{lim} for the clamped box in compression and several values of t/a.

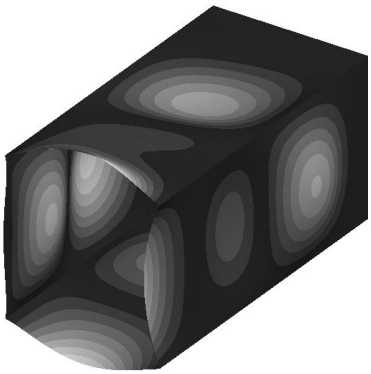

Figure 10: Shape of the worst imperfection for the box in compression, with $t/a = 1/400$.

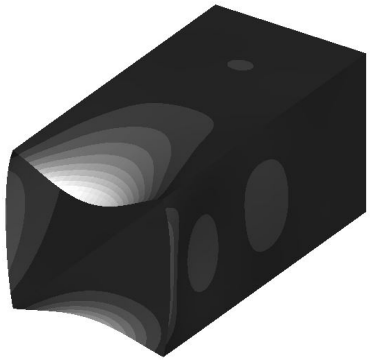

Figure 11: Mode shape at minimum limit load with the worst imperfection for the box in compression, with $t/a = 1/400$.

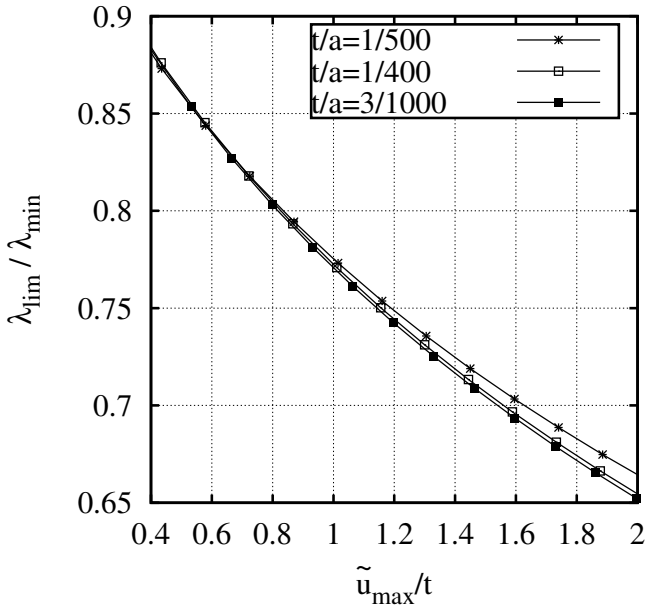

Figure 12: Load sensitivity to worst imperfection amplitude $\tilde{u}_{max}/t$ for the box in compression at several values of t/a.

7.2. Imperfection sensitivity analysis of cylindrical shell

The proposed methodology for imperfection sensitivity analysis is general in the sense that it can be applied to any type of slender structure. The particular FE formulation used in this work is based on a flat shell finite element (MISS-4,[14]) that is particularly suitable for the analysis of folded plates [32]. However, curved shells can be analyzed using MISS-4 by approximating the curved shell as a collection of small flat elements with characteristic size h, retaining h^2 convergence of the solution, as shown in [14, Section 4.3].

In this section, two cylinders labeled Z32 and Z33 [43], are analyzed. These cylinders have been applied as benchmark cases of imperfection sensitivity [27, 44–47]. The ply properties are $E_1 = 123.6$ GPa; $E_2 = 8.7$ GPa; $G = 5.7$ GPa; $\nu_{12} = 0.32$. The laminate stacking sequence is ${}_{IN}[-51/51/-45/45/-37/37/-19/19/0/0]_{OUT}$ and ${}_{IN}[0/0/19/-19/37/-37/45/-45/51/-51]_{OUT}$ for Z32 and Z33, respectively. The height is $510\,mm$, the radius $R = 250\,mm$ and the laminate thickness $t = 1.25\,mm$. In addition to the radius/thickness $R/t = 200$, the ratios $R/t = 50, 100, 400, 800$ have been analysed.

The cylinders are clamped on top and bottom, except for the axial displacement at the top edge, which is free to allow the application of a distributed load. The imperfection sensitivity analysis has been carried out for different radius versus thickness ratio. A mesh of square elements (6.8×6.8 mm) is used for all cases.

The results on buckling loads are reported in Tables 2 and 3. Buckling modes are shown in Figure 13, and the quadratic correction functions are shown in Figure 14. Eight buckling modes have been considered for the multi-modal analysis. The limit load distribution considering one thousand imperfections with maximum amplitude $\tilde{u}_{max}/t = 0.2$ is shown in Figure 15. The shape of the worst imperfection and the deformed shape at minimum limit load are shown in Figures 16 and 17, respectively. The load sensitivity as a function of the amplitude of the worst imperfection is reported in Figure 18, where it can be seen that cylinder Z33 is more imperfection sensitive that Z32.

R/t	λ_1	λ_2	λ_3	λ_4	λ_5	λ_6	λ_7	λ_8
50	1680.540	1689.500	1701.370	1701.370	1722.910	1722.890	1771.550	1771.560
100	411.049	413.328	413.613	413.612	417.888	417.891	422.512	422.514
200	103.349	103.562	103.578	103.578	104.278	104.278	104.662	104.660
400	26.744	26.756	26.756	26.767	26.885	26.885	26.887	26.886
800	7.215	7.215	7.217	7.220	7.231	7.231	7.242	7.242

Table 2: Buckling loads (in kN) for cylinder Z32 as a function of radius/thickness ratio.

R/t	λ_1	λ_2	λ_3	λ_4	λ_5	λ_6	λ_7	λ_8
50	3195.180	3195.200	3305.300	3305.820	3312.270	3313.840	3355.110	3355.580
100	800.113	800.100	800.496	800.497	804.968	804.982	824.417	825.567
200	199.055	199.055	200.314	200.313	201.449	201.454	202.234	202.236
400	50.578	50.578	50.579	50.579	50.674	50.674	51.056	51.056
800	12.945	12.945	12.957	12.957	13.034	13.034	13.066	13.066

Table 3: Buckling loads (in kN) for cylinder Z33 as a function of radius/thickness ratio.

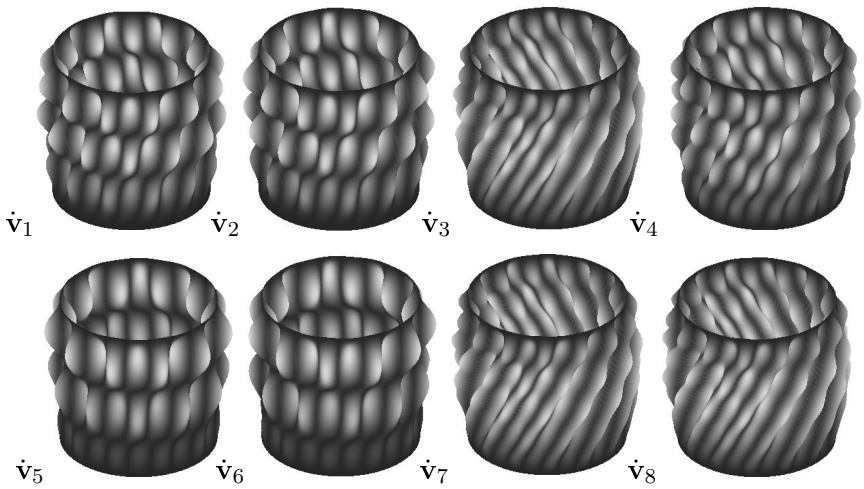

Figure 13: Buckling modes for cylinder Z33 with $R/t = 200$.

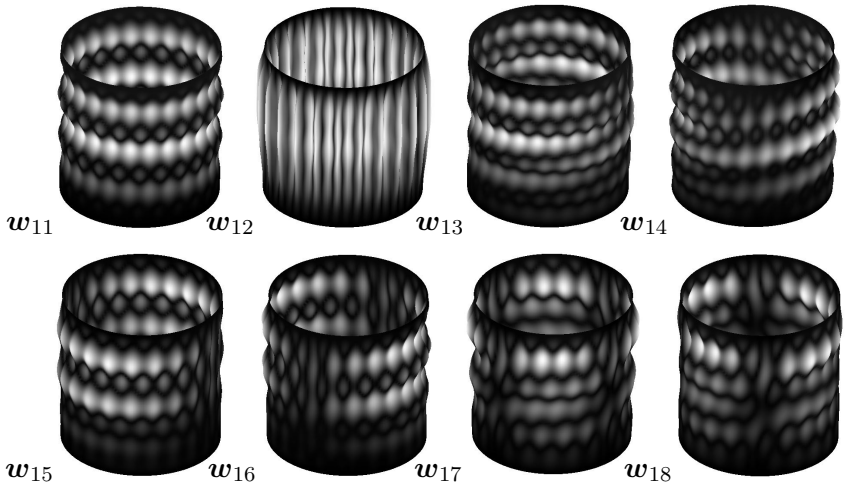

Figure 14: Quadratic corrections for cylinder Z33 with $R/t = 200$.

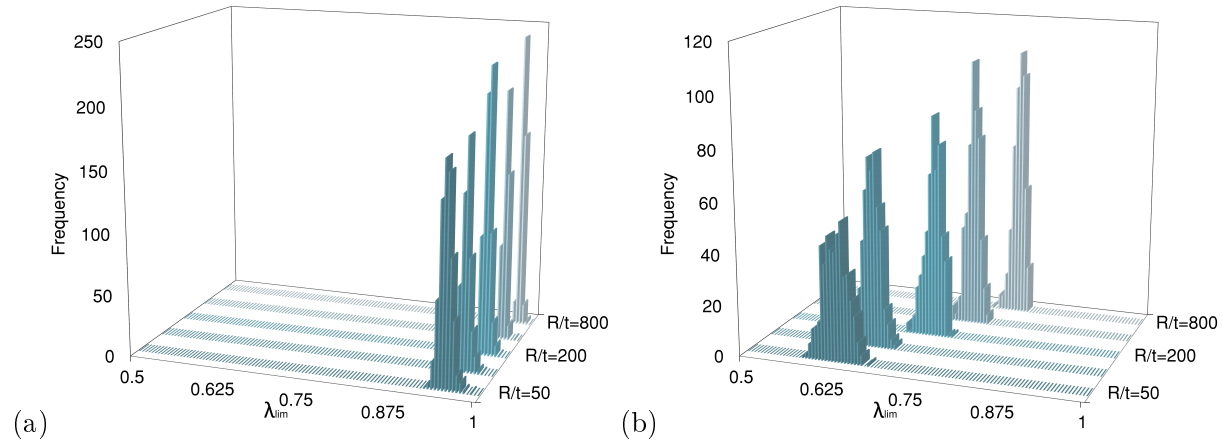

Figure 15: Frequency distribution of the lowest limit load λ_{lim} for cylinders (a) Z32 and (b) Z33 at several values of radius-to-thickness ratios.

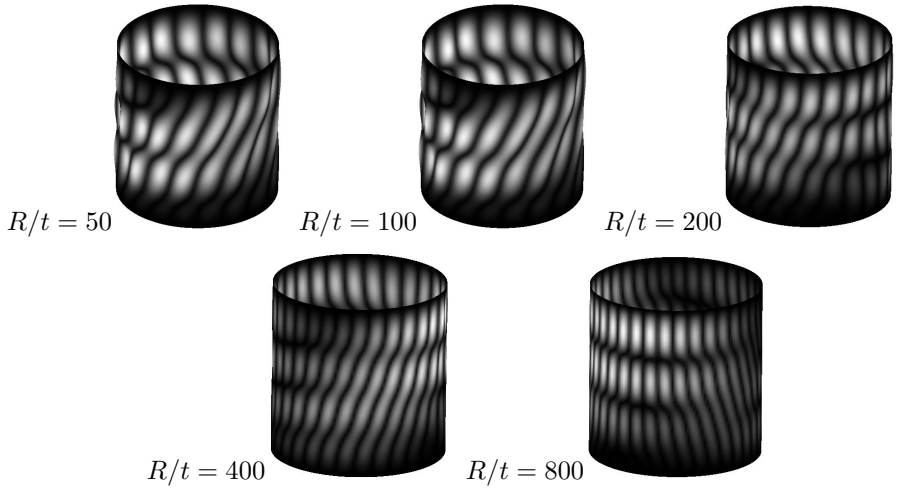

Figure 16: Shapes of the worst imperfection for cylinder Z33 at several radius-to-thickness ratios.

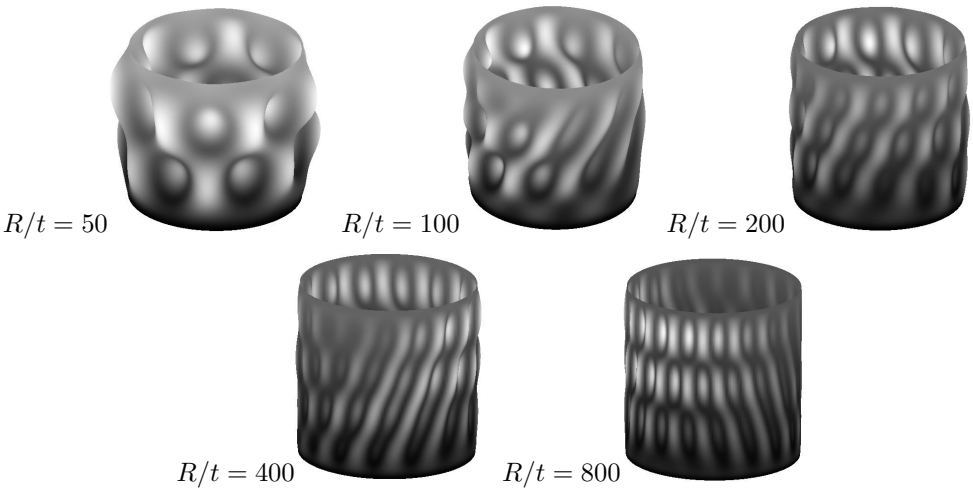

Figure 17: Mode shapes at minimum limit load with the worst imperfection for cylinder Z33 and several radius-to-thickness ratios.

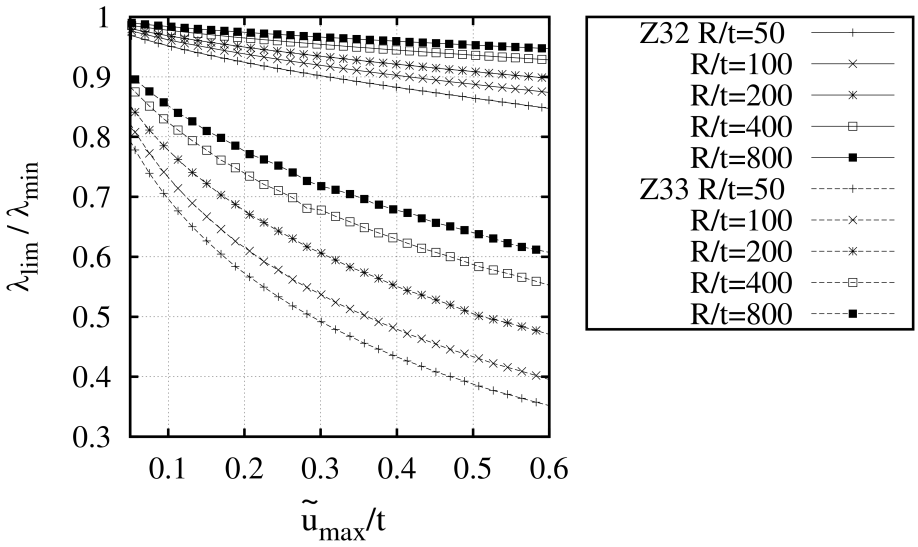

Figure 18: Limit load sensitivity to worst imperfection amplitude for cylinders Z32 and Z33 and several radius-to-thickness ratios.

7.2.1. Remarks

The imperfection sensitivity analysis in the context of Koiter's approach allows us to perform Monte Carlo simulation with very low computational cost. Analysis time is reported in Table 4. The computations are performed on a Intel(R) Xeon(R) CPU E5-2620 2.00Ghz Dual Core, 32 GB Ram on a single core. Each value in Table 4 requires the solution of eq. (1h) for as many random imperfections as indicated in the heading for that column.

The average time required for the steps i. to iv. have been studied [10], and they remain of the order of seconds. The times are also a few seconds for a very large number of imperfections. This could allow users to run Monte Carlo simulations to account for other types of imperfections (i.e., load imperfection, residual stress, and so on) in order to obtain even more realistic evaluations of structural performance.

For the example studied, an imperfection in the shape of the first buckling mode (see $\dot{\boldsymbol{v}}$ in Figure 13) does not necessarily produce the worst imperfection (see Figure 16). Also, the buckling modes for minimum limit load do not resemble the worst imperfection. These observations provide empirical justification for performing a full exploration of the imperfection space, as proposed in this work.

The accuracy, robustness, and reliability of the results are closely related to the use of geometrically exact structural models and mixed formulation. The latter is necessary to prevent extrapolation locking phenomena [13]. The use of a corotational formulation coupled with a mixed finite element allows to easily satisfy these requirements. Moreover, Koiter's approach being based on asymptotic expansion, allows to recover the equilibrium path in an approximate fashion. The best accuracy is available for the pre-critical and the initial post-critical behavior. A numerical comparison between Riks' and Koiter's method for the recovery a single equilibrium path, as implemented in this paper, can be found in [8–10].

The accuracy of imperfection sensitivity of Koiter's analysis compared to Riks' analysis are shown (numerically) in Figure 19. The path-following solution is obtained using Riks' standard implementation in Abaqus [48] along with Abaqus' S4R elements. The accuracy of our implementation of Koiter's method (Section 2) decreases with the imperfection amplitude. This is due to the fact that the imperfections are incorporated during post-processing, i.e. eq. (1h), in order to keep the computational cost to a minimum. A method for improving the imperfection amplitude

range of Koiter's method is reported by [49] along with an extensive discussion on calculations of imperfection sensitivity curves for unstiffened and stiffened cylinders is also reported.

	Time (s)				
R/t	100 imp.	500 imp.	1000 imp.	5000 imp.	10000 imp.
50	18.011	89.688	270.346	5344.72	10764.88
100	14.403	67.853	242.540	5434.89	10599.07
200	14.643	77.345	249.089	5350.40	10480.74
400	19.964	97.050	285.614	5275.00	10193.00
800	11.652	60.923	217.769	5106.57	10694.88

Table 4: Computational cost for cylinder Z33 and several radius-to-thickness ratios. The cost refers to the solution of equation (1h).

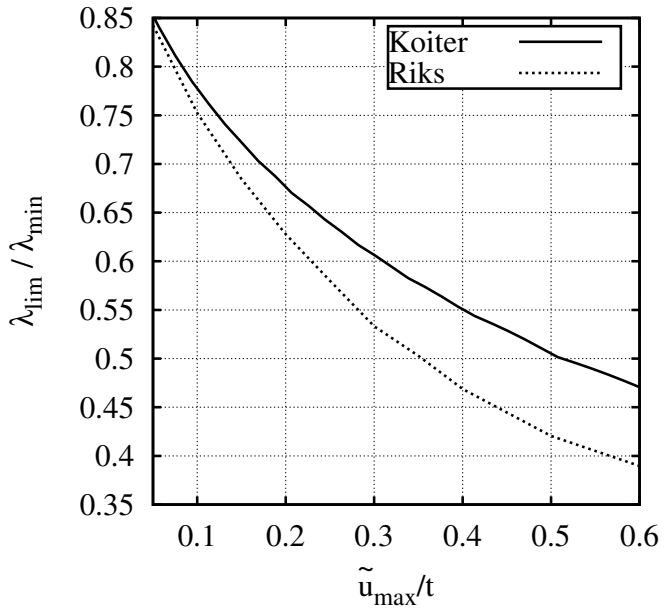

Figure 19: Load sensitivity to worst imperfection $\tilde{u}_{max}$ for cylinder Z33 with $R/t = 200$.

8. CONCLUSIONS

The advantages of using Koiter's asymptotic approach for the analysis of slender elastic structures has been shown. The possibility of performing an efficient and reliable imperfection sensitivity analysis, including cases with modal interaction, based on Monte Carlo simulation has been demonstrated. The computational cost needed to account for a large sample of imperfections is, on average, in the range of a few seconds. The worst imperfections can be detected without a-priori knowledge about the shape of such imperfections. The load capacity can evaluated statistically and its sensitivity to the amplitude of the worst imperfection can be calculated easily.

Acknowledgement

Special recognition is due to Prof. Raffaele Casciaro for his suggestions and comments. The authors from University of Calabria wish to acknowledge the *International Network for the Exchange of Good Practices in Innovative, Seismically Safe and Eco-friendly Buildings* (POR-FSE CALABRIA 2007-2013 RISPEISE) for the financial support.

[1] Daoud F, Calomfirescu M. Optimization of Composite Aircraft Structures in Consideration of Postbuckling Behavior. Int J Str Stab Dyn 2010; 10(4):905-916.

[2] Degenhardt R, Castro SGP, Arbelo MA, Zimmerman R, Khakimova R, Kling A. Future structural stability design for composite space and air frame structures. Thin Wall Struct 2014; 81:29-38.

[3] Riks E. An incremental approach to the solution of snapping and buckling problems. Int J Solids Struct 1979; 15(7):529-551.

[4] Kouhia R, Mikkola M. Tracing the equilibrium path beyond compound critical points. Int J Numer Meth Eng 1999; 46(7):1049-1074.

[5] Koiter WT. On the stability of elastic equilibrium. 1945; English transl. NASA TT-F10, 883 (1967) and AFFDL-TR70-25 (1970).

[6] Casciaro R. Computational asymptotic post-buckling analysis of slender elastic structures. Phenomenological and Mathematical Modelling of Structural Instabilities, Springer Vienna 2005; 470:195-276.

[7] Barbero EJ. Prediction of Compression Strength of Unidirectional Polymer Matrix Composites. J Compos Mater 1998; 32(5):483-502.

[8] Garcea G, Madeo A, Zagari G, Casciaro R. Asymptotic post-buckling FEM analysis using corotational formulation. Int J Solids Struct 2009; 46(2):377-397.

[9] Zagari G, Madeo A, Casciaro R, de Miranda S, Ubertini F. Koiter analysis of folded structures using a corotational approach. Int J Solids Struct 2013; 50(5):755-765.

[10] Barbero EJ, Madeo A, Zagari G, Zinno R, Zucco G. Koiter asymptotic analysis of folded laminated composite plates. Composites Part B 2014; 61:267-274.

[11] Garcea G, Madeo A, Casciaro R. The implicit corotational method and its use in the derivation of nonlinear structural models for beams and plates. J Mech Mat Struct 2012; 7(6):509-538.

[12] Garcea G, Madeo A, Casciaro R. Nonlinear FEM analysis for beams and plate assemblages based on the Implicit Corotational Method. J Mech Mat Struct 2012; 7(6):539-574.

[13] Garcea G, Salerno G, Casciaro R. Sanitizing of locking in Koiter perturbation analysis through mixed formulation. Comput Method Appl M 1999; 180:137-167.

[14] Madeo A, Zagari G, Casciaro R, Miranda S. A Mixed 4-Node 3D plate Element Based on Self-Equilibrated Isostatic Stresses. Int J Str Stab Dyn 2014; DOI: 10.1142/S0219455414500667

[15] Madeo A, Zagari G, Casciaro R. An isostatic quadrilateral membrane finite element with drilling rotations and no spurious modes. Finite Elem Anal Des 2012; 50:21-32

[16] Godoy LA. Theory of Elastic Stability-Analysis and Sensitivity. Taylor and Francis 1999.

[17] Barbero EJ. Prediction of Buckling-Mode Interaction in Composite Columns. Mech Compos Mater St 2000; 7:269-284.

[18] Barbero EJ, Dede E, Jones S. Experimental Verification of Buckling-Mode Interaction in Intermediate-Length Composite Columns. Int J Solids Struct 2000; 37:3919-3934.

[19] Garcea G., Bilotta A, Madeo A, Casciaro R. Direct evaluation of the post-buckling behaviour of slender structures through a numerical asymptotic formulation. Direct Methods for Limit States in Structures and Materials 2014; 203-228.

[20] Salerno G, Casciaro R. Mode jumping and attrative paths in multimode elastic buckling. Int J Numer Meth Eng 1997; 40:833-861.

[21] Salerno G, Uva G. Ho's theorem in global−local mode interaction of pin-jointed bar structures. Int J Nonlinear Mech 2006; 41(3):359-376.

[22] Casciaro R, Mancusi G. Imperfection sensitivity due to coupled local instability: a non-convex QP solution algorithm. Int J Numer Meth Eng 2006; 67(6):815-840.

[23] Dubina D. The ECBL approach for interactive buckling of thin-walled steel members. Steel and Composite Structures 2001; 1(1):75-96.

[24] Dubina D, Ungureanu V. Effect of imperfections on numerical simulation of instability behaviour of cold-formed steel members. Thin Wall Struct 2002; 40(3):239-262.

[25] Dubina D, Ungureanu V. Instability mode interaction: From Van Der Neut model to ECBL approach. Thin Wall Struct 2014; 81:39-49.

[26] Castro SGP, Zimmermann R, Arbelo MA, Khakimova R, Hilburger MW, Degenhardt R. Geometric imperfections and lower-bound methods used to calculate knock-down factors for axially compressed composite cylindrical shells. Thin Wall Struct 2014; 74:118-132.

[27] Arbelo MA, Degenhardt R, Castro SGP, Zimmermann R. Numerical characterization of imperfection sensitive composite structures. Compos Struct 2014; 108:295-303.

[28] Orifici AC, Bisagni C. Perturbation-based imperfection analysis for composite cylindrical shells buckling in compression. Compos Struct 2013; 106:520-528.

[29] Reddy JN. Mechanics of laminated composite plates and shells-theory and analysis. CRC Press, 2nd ed., 2004.

[30] Barbero EJ. Introduction to Composite Materials Design. CRC, Boca Raton, FL, second edition, 2011.

[31] de Miranda S, Ubertini F. A simple hybrid stress element for shear deformable plates. Int J Numer Meth Eng 2006; 65(6):808-833.

[32] Barbero EJ, Madeo A, Zagari G, Zinno R, Zucco G. A mixed isostatic 24 dof element for static and buckling analysis of laminated folded plates. Compos Struct 2014; 116:223-234.

[33] Rankin CC, Nour-Omid B. The Use of Projectors to Improve Finite Element Performance. Elsevier 1998; 257-267.

[34] Nour-Omid B, Rankin CC. Finite rotation analysis and consistent linearization using projectors. Comput Method Appl M 1991; 93(3):353-384.

[35] Mostafa M, Sivaselvan MV, Felippa CA. A solid-shell corotational element based on ANDES, ANS and EAS for geometrically nonlinear structural analysis. Int J Numer Meth Eng 2013. 95(2):145-180.

[36] Mostafa M, Sivaselvan MV, Felippa CA. Reusing linear finite elements in material and geometrically nonlinear analysis-Application to plane stress problems. Finite Elem Anal Des 2013; 69:62-72.

[37] Caselli F, Bisegna P. Polar decomposition based corotational framework for triangular shell elements with distributed loads. Int J Numer Meth Eng 2013; 95(6):499-528.

[38] Li ZX, Liu YF, Izzuddin BA, Vu-Quoc L. A stabilized co-rotational curved quadrilateral composite shell element. Int J Numer Meth Eng 2011; 86(8):975-999.

[39] Li ZX, Zhuo X, Vu-Quoc L, Izzuddin BA, Wei HY. A four-node corotational quadrilateral elastoplastic shell element using vectorial rotational variables. Int J Numer Meth Eng 2013; 95(3):181-211.

[40] Norachan P Suthasupradit S, Kim KD. A co-rotational 8-node degenerated thin-walled element with assumed natural strain and enhanced assumed strain. Finite Elem Anal Des 2012; 50:70-85.

[41] Rodrigues O. Des lois géométriques qui régissent les déplacements d'un système solide dans l'espace, et de la variation des coordonnées provenant de ces déplacements considérés indépendamment des causes qui peuvent les produire. J Math Pure Appl 1840; 5:380-440.

[42] Bilotta A, Casciaro R. Assumed stress formulation of high order quadrilateral elements with an improved in-plane bending behaviour. Comput Method Appl M 2002; 191(15-16):1523-1540.

[43] Castro SGP, Zimmermann R, Arbelo MA, Degenhardt R. Exploring the constancy of the global buckling load after a critical geometric imperfection level in thin-walled cylindrical shells for less conservative knock-down factors. Thin Wall Struct 2013; 72:76-87.

[44] Arbelo MA, de Almeida SFM, Donadon MV, Rett SR, Degenhardt R, Castro SGP, Kalnins K, Ozoliņš O. Vibration correlation technique for the estimation of real boundary conditions and buckling load of unstiffened plates and cylindrical shells. Thin Wall Struct 2014; 79:119-128.

[45] Castro SGP, Mittelstedt C, Monteiro FAC, Arbelo MA, Degenhardt R, Ziegmann G. A semi-analytical approach for linear and non-linear analysis of unstiffened laminated composite cylinders and cones under axial, torsion and pressure loads. Thin Wall Struct 2015; DOI 10.1016/j.tws.2015.01.002.

[46] Arbelo MA, Herrmann A, Castro SGP, Khakimova R, Zimmermann R, Degenhardt R. Investigation of buckling behavior of composite shell structures with cutouts. Appl Compos Mater 2014; DOI 10.1007/s10443-014-9428-x.

[47] Castro SGP, Mittelstedt C, Monteiro FAC, Degenhardt R, Ziegmann G. Evaluation of non-linear buckling loads of geometrically imperfect composite cylinders and cones with the Ritz method. Compos Struct 2015; 122:284-289.

[48] Hibbitt, Karlsson, Sorensson. Abaqus theory manual, version 6.8, Dassault 2009.

[49] Xu H. Buckling, Postbuckling and Imperfection Sensitivity Analysis of Different Type of Cylindrical Shells by Hui's Postbuckling Method. University of New Orleans Theses and Dissertations 2013, Paper 1781.